Preparation and *in vitro* study of stromal cell-derived factor 1-targeted Fe_3O_4/poly(lactic-co-glycolic acid)/perfluorohexane nanoparticles

FEI WANG[1-3], ZHIGANG WANG[3], LIANG PANG[1,2], SHULIANG WAN[1-3] and LIHUA QIU[1,2]

[1]Depatment of Oral and Maxillofacial Surgery, Stomatological Hospital Affiliated to Chongqing Medical University; [2]Chongqing Municipal Key Laboratory of Oral Biomedical Engineering of Higher Education, Chongqing Medical University, Chongqing 401147; [3]Chongqing Key Laboratory of Ultrasound Molecular Imaging, Chongqing Medical University, Chongqing 400010, P.R. China

Received December 5, 2019; Accepted April 29, 2020

DOI: 10.3892/etm.2020.8925

Abstract. Compared with traditional imaging techniques, multimodal imaging obtains more accurate images that may increase disease detection rates. The present study prepared stromal cell-derived factor 1 (SDF-1)-loaded, targeted nanoparticles coated with iron (II,III) oxide and perfluorohexane (PFH) to be used as polymer-shelled contrast agents with multimodal imaging functions, with the aim of improving tongue cancer and lymph node metastasis diagnosis. The multifunctional, targeted, polymeric nanoparticles were prepared using a double emulsion method and chemokine SDF-1 was conjugated to nanoparticles by a sulfide bond. The nanoparticles were spherical, uniform size and well dispersed. The results of the *in vitro* photoacoustic and ultrasonic imaging experiments demonstrated that the multifunctional nanoparticles displayed excellent multimodal imaging functions, as even small concentrations of nanoparticles presented clear ultrasound and photoacoustic imaging. When the temperature reached the boiling point of PFH (56˚C), a liquid-gas phase change occurred and the microsphere volume and acoustic impedance increased, leading to enhanced ultrasonic development. The nanoparticles were automatically targeted to tongue squamous carcinoma cells *in vitro* via SDF-1-CXC chemokine receptor 4 interactions. The targeted experiment and flow cytometry results indicated that the nanoparticles underwent strong targeted binding to human tongue squamous cell carcinoma (SCC-15) cells. In summary, the nanoparticles were automatically targeted to SCC-15 cells and displayed promising characteristics for ultrasound and photoacoustic imaging. Higher concentrations of nanoparticles was associated with clearer imaged and greater echo intensity value and photoacoustic value. The present study established a foundation for the development of procedures for primary tongue cancer and lymph node metastasis diagnosis.

Correspondence to: Professor Lihua Qiu, Department of Oral and Maxillofacial Surgery, Stomatological Hospital Affiliated to Chongqing Medical University, 426 Songshi North Avenue, Chongqing 401147, P.R. China
E-mail: 500082@hospital.cqmu.edu.cn

Key words: superparamagnetic iron oxide, targeted nanoparticles, contrast agent, multimodal imaging, tongue squamous cell carcinoma

Introduction

A total of 90% of all cases of oral cancer are classified as squamous cell carcinoma (SCC), with SCC of the tongue comprising 50-60% cases worldwide, making it the most common type of oral cancer (1,2). Tongue cancer can metastasize from the primary site to cervical regional lymph nodes in the early stage (3), resulting in a 5-year survival rate of <50% (4,5). Therefore, the early diagnosis and treatment of cervical lymph node metastasis in patients with SCC of the tongue is crucial in order to improve patient survival rates.

The treatment of oral cancer typically includes surgery, post-operative adjuvant radiotherapy and chemotherapy (6). Pre-operative ultrasound is a non-invasive method used to examine lymph nodes; however, ultrasound cannot distinguish lymphadenitis from metastatic lymph nodes (7). Moreover, the current imaging strategies often result in a missed diagnosis or misdiagnosis of cancer, especially in patients with early metastatic lymphoma (8,9). Establishing reliable diagnostic procedures and standards for the primary foci of tongue cancer and the detection of metastatic SCC in lymph nodes has important potential diagnostic and prognostic value for patients with oral cancer.

Multimodal imaging has become a frequently used technique in molecular imaging as it can be used to obtain more accurate images and improve the detection rate of diseases, including thyroid cancer (10) and liver fibrosis (11). There has been an increased interest worldwide in nano-composite materials with multimodal imaging functions (12-14). Poly(lactic-co-glycolic acid)(PLGA) is commonly used in the preparation of ultrasound contrast agents. PLGA is a biodegradable organic polymer compound with hydrophobic properties,

high spheronization, film formation rates and good biocompatibility (15,16). As a Food and Drug Administration-approved material, PLGA has been widely used in protein research and clinical applications for the delivery of small molecule drugs and other large molecules (17).

Liquid fluorocarbon perfluorohexane (PFH) is an aliphatic fluorine-containing compound with a low boiling point (56˚C) (6). PFH displays good biocompatibility and is eliminated directly via respiration without degradation *in vivo* (18). Furthermore, the diameter of a nanoparticle contrast agent coated with liquid fluorocarbon can be increased following liquid-gas phase change, which results in increased acoustic impedance followed by increased enhanced ultrasonic signal development (19).

Superparamagnetic iron oxide (SPIO) nanoparticles can be coated with a variety of biological macromolecules due to their small particle size and strong surface modifiability (20). Additionally, SPIO nanoparticles display good biological safety and a long circulation half-life (21). SPIOs integrate magnetic resonance (MR), ultrasonic and photoacoustic (PA) multimodal imaging, providing novel ideas and strategies for disease diagnosis and treatment (22-26). Norton *et al* (27) demonstrated that magnetic SPIO particles vibrate under the action of acoustic waves, which alters the acoustic impedance of tissues and enhances backscatter signals and ultrasound imaging. A previous study reported that PA imaging technology based on the PA effect has received increasing interest (28). PA imaging technology is a safe and nondestructive imaging technology that uses a pulsed laser as the excitation source to irradiate the medium with a light absorber to generate a PA effect. Moreover, the imaging method reconstructs and calculates the collected acoustic signals via a signal processing system to obtain information regarding the internal structure of tissues (29).

PA imaging technology combines the advantages of pure optical and acoustic imaging of tissues, thus obtaining tissue images with high contrast and spatial resolution (30). As a light absorber, SPIO can absorb laser light at specific wavelengths (31). Laser irradiation of SPIO-coated particles causes the temperature of the surrounding medium to rise, causing the medium to expand, generating PA signals (32).

The specific receptor for stromal cell-derived factor (SDF)1 is CXC chemokine receptor 4 (CXCR4), which is expressed by fibroblasts, endothelial cells, some inflammatory cells (natural killer cells, neutrophils, plasma cells and B and T lymphocytes) and various cancer cells (33). Delilbasi *et al* (34) demonstrated that all tongue SCC cells expressed CXCR4 whereas normal squamous epithelium had no or little expression of CXCR4 and that metastatic SCC cells from the lymph nodes displayed stronger expression compared with lymphocytes. At present, CXCR4 is the only known receptor of SDF-1 (6).

The CXCR4-C-X-C motif chemokine (CXCL)12 axis serves an important role in the invasion and metastasis of SCC and has been indicated to contribute to tumor development. Due to this (35), it is often used as a potential target in SCC treatment (36).

The aim of the present study was to prepare SDF-1-modified nanoparticle contrast agents coated with iron (II,III) oxide (Fe_3O_4), the main component of SPIO (21) and PFH for targeted multi-modal imaging and to examine their properties *in vitro*. The present study provided a potential foundation for the development of procedures and materials for the diagnosis of primary tongue cancer and lymph node metastasis.

Materials and methods

Materials. Fe_3O_4 (cat. no. SOR-10-50) modified by oleic acid was obtained from Ocean NanoTech, LLC. Maleimide-polyethylene glycol-poly(lactide co-glycolide)(MAL-PEG-PLGA; 75:25; 12,000 Da MW) was purchased from Jinan Daigang Biomaterial Co., Ltd. Polyvinyl alcohol (PVA; 25,000 Da) and PFH were obtained from Sigma-Aldrich, Merck KGaA. Methylene chloride (CH_2Cl_2) and isopropyl alcohol were purchased from Chongqing East Sichuan Chemical Co., Ltd. SDF-1 modified with FITC was obtained from Shanghai Qiangyao Biotechnology Co., Ltd. The human tongue SCC cell line (SCC-15) was obtained from the Chongqing Key Laboratory of Oral Diseases and Biomedical Sciences.

Preparation of SDF-1/Fe_3O_4/PLGA/PFH nanoparticles. A double emulsification method was used to prepare PLGA shells loaded with Fe_3O_4 and PFH. A total of 100 mg PLGA and 5 mg Fe_3O_4 were added into 2 ml CH_2Cl_2 and the mixture was placed in an ice bath with an ultrasound probe at 125 W for 60 sec until it was fully dissolved. Subsequently, 100 μl PFH and 5 ml of 50 g/l PVA were added to the emulsion, followed by ultrasound treatment for 5 min (on: 5 sec; off: 5 sec) in an ice bath to obtain the first emulsion. A total of 10 ml isopropyl alcohol (20 ml/l) was then poured into the first emulsion to solidify the surface of the nanoparticles. A total of 2 magnetic beads (Beyotime Institute of Biotechnology,) were placed into the mixture and the liquid was stirred on a magnetic stirrer for 3 h in an ice bath to extract CH_2Cl_2. The sample was then centrifuged with pure water in a low-temperature (4˚C) high-speed centrifuge (5 min; 9,391 x g) and the supernatant was discarded. The precipitate was washed with pure water and the process was repeated in triplicate. A total of 200 μl SDF-1 (terminal sulfhydrylation modification and FITC labeling) was added into the final emulsion and stirred for 4 h at 4˚C. SDF-1 was conjugated to nanoparticles via thioether bonds. Particles were then centrifuged at 9,391 x g for 5 min at 4˚C and washed with pure water. The process was repeated twice to obtain SDF-1/Fe_3O_4/PLGA/PFH nanoparticles, which were stored in the dark at 4˚C until further analysis.

The blank PLGA nanoparticles, Fe_3O_4/PLGA/PFH nanoparticles and SDF-1/PLGA/PFH nanoparticles were all prepared according to the aforementioned method.

Determination of the basic properties of the SDF-1/Fe_3O_4/PLGA/PFH nanoparticles. Samples were gently stirred with a pipette until they were fully dispersed and assessed for surface morphology, distribution and size using a CKX41 light microscope (magnification, x100); Olympus Corporation) and a JEOL JSM-7800F scanning electron microscope (magnification, x2,000; Hitachi, Ltd.). A drop of the nanoparticles (50 ug/ml) was placed on a silicon panel (5x5 mm) until it dried naturally in the dark overnight at room temperature. The silicon panel then analyzed via scanning electron microscopy. A TCS-SP5 laser confocal microscopy (magnification, x400; Leica Microsystems GmbH) was used

to observe SDF-1 conjugation. A laser particle size meter (Zetasizer 3000HS; Malvern Instruments, Inc.) was used to detect particle size and Zeta potential. Determination of the iron content in the samples (3) was performed via graphite furnace atomic absorption spectrometry. The wavelength used for detection was 248.3 nm. The absorption spectrum of the nanoparticles was detected using an ultraviolet-visible (UV-Vis) spectrophotometer (CARY 50; Varian Medical Systems) and blank PLGA nanoparticles were used as the control group.

In vitro imaging experiments. The absorption peaks of nanoparticles were measured by UV-Vis spectrophotometry, which was performed in previous experiments (21). The absorption peaks provided the basis for selecting the excitation laser wavelength for PA imaging experiments. The SDF-1/Fe_3O_4/PLGA/PFH, Fe_3O_4/PLGA/PFH, SDF-1/PLGA/PFH and blank PLGA nanoparticles were divided into 4 groups according to PLGA concentration (20, 15, 10 and 5 mg/ml). A total of 200 μl of mixture from each group was placed in 3% agarose gel phantoms and the PA images and signals values of the groups were collected at the optimal wavelength (680 nm) using a VEVO LAZR PA imaging system (Vevo® LAZR; FUJIFILM VisualSonics, Inc.).

Ultrasonic imaging experiment. Ultrasound images of SDF-1/Fe_3O_4/PLGA/PFH nanoparticles were recorded according to 4 different PLGA concentrations (100, 50, 25 and 12.5 mg/ml) at a mechanical index (MI) of 0.6 and under different MIs (0.2-0.6) at the PLGA concentration of 12.5 mg/ml using an ultrasound apparatus (Philips iU22; Philips Healthcare). A total of 1 ml SDF-1/Fe_3O_4/PLGA/PFH nanoparticles were injected into a transparent rubber tube and placed into a water bath with an initial temperature of 37˚C for 6 min to obtain the images. During the process, the temperature was slowly raised (to 65˚C) and monitored in real time. Using the B-mode and contrast mode of the ultrasound apparatus, images of SDF-1/Fe_3O_4/PLGA/PFH nanoparticles were obtained at the temperature of 56˚C when the two-dimensional grayscale ultrasound imaging and contrast-enhanced ultrasound imaging were strongest. The blank PLGA nanoparticles were treated using the same method. A DFY ultrasonic image quantitative analysis diagnostic instrument (Sonomath; Chongqing Ambition Science & Technologies Co., Ltd.) measured the echo intensity (EI) value of the samples. Additionally, alterations to SDF-1/Fe_3O_4/PLGA/PFH nanoparticle volume in response to increasing temperature were observed and recorded via an IX71 light microscope (magnification, x40; Olympus Corporation).

Cell culture. SCC-15 cells were cultured in DMEM/Nutrient Mixture F-12 (DMEM-12; Gibco; Thermo Fisher Scientific, Inc.) containing 10% FBS (Gibco; Thermo Fisher Scientific, Inc.) and 1% penicillin or streptomycin at 37˚C with 5% CO_2. The culture medium was changed every 2 days. At 80% confluence, cells were sub-cultured as follows: The culture medium was removed, cells were washed with PBS 3 times, 1 ml 0.25% trypsin was added and cells were returned to the incubator for 5 min. A total 3 ml DMEM-12 culture medium was added to the cells for neutralization. The mixture was pipetted up and down to form a well-mixed suspension and centrifuged for 3 min at 200 x g and 4˚C. The supernatant was removed and cells were resuspended in DMEM-12 medium.

Detection of CXCR4 localization and expression of SCC-15 cells. SCC-15 cells in the logarithmic phase were digested with 1 ml 0.25% trypsin for 5 min and then centrifuged at 200 x g for 3 min at 4˚C. Subsequently, cells were inoculated ($5x10^4$ cells/well) into 6-well plates with coverslips. Cells were cultured in DMEM-12 medium and incubated overnight with 5% CO_2 at 37˚C. Cells were washed twice with PBS, fixed with 4% paraformaldehyde for 15 min at room temperature, washed with PBS 3 times and blocked with goat serum blocking solution (1% BSA; Beyotime Institute of Biotechnology) at 37˚C for 30 min to block non-specific antibody binding. Subsequently, rabbit anti-human CXCR4 primary antibody (1:200) was added to the cover glass, which was incubated at 4˚C overnight. After washing 3 times with PBS, FITC-labelled goat anti-rabbit IgG secondary antibody (1:100; A0562; Beyotime Institute of Biotechnology) was added to the cells and incubated at 37˚C for 50 min in the dark. After rinsing 3 times with PBS, cells were stained with DAPI for 5 min at room temperature, washed 3 times with PBS and stored at -20˚C until observation. Cells were observed under a TCS-SP5 laser confocal microscopy (magnification, x200; Leica Microsystems GmbH).

Targeted experiment. SCC-15 cells in the logarithmic phase were inoculated ($1x10^5$ cells/dish) into a 15 mm laser confocal dish. Cells were divided into 2 groups: i) SDF-1/Fe_3O_4/PLGA/PFH nanoparticle group; and ii) the blank control group. A total of 2 ml DMEM-12 medium was added to each dish. Following incubation for 12 h, the medium in the dish was changed. A total of 2 ml nanoparticles prepared in DMEM-12 (200 μg/ml) was added to the experimental group and 2 ml DMEM/F-12 medium was added to the blank control group. Following incubation for 2 h at 37˚C, cells were washed once with PBS and nanoparticle targeting was observed using a fully automatic fluorescence microscope (magnification, x200; Axio Imager.Z2; Carl Zeiss AG).

Flow cytometry test. SCC-15 cells in the logarithmic phase were inoculated ($1x10^6$ cells/well) into 6-well plates. Cells were divided into 2 groups: i) SDF-1/Fe_3O_4/PLGA/PFH nanoparticle group; and ii) the blank control group. A total of 2 ml DMEM-12 medium was added to each dish. Following incubation for 12 h at 37˚C, the medium in the dish was changed. A total of 2 ml nanoparticles prepared in DMEM/F-12 medium (200 μg/ml) was added to the experimental group and 2 ml DMEM/F-12 medium was added to the blank control group. Following incubation for 2 h at 37˚C, cells were washed 3 times with PBS, digested with 0.25% pancreatin for 5 min, centrifuged 3 times at 200 x g for 3 min at 4˚C and the obtained precipitate was resuspended in PBS for flow cytometry (BD INFLUX; Becton, Dickinson and Company). Nanoparticles with SDF-1 were selected as the analyte detector and FITC was used as the analyte reporter. FlowJo software (version 7.6.5; Becton, Dickinson and Company) was used for the analysis of flow cytometer data.

Statistical analysis. Statistical analyses were performed using SPSS software (version 22.0; IBM Corp.). Data are presented as

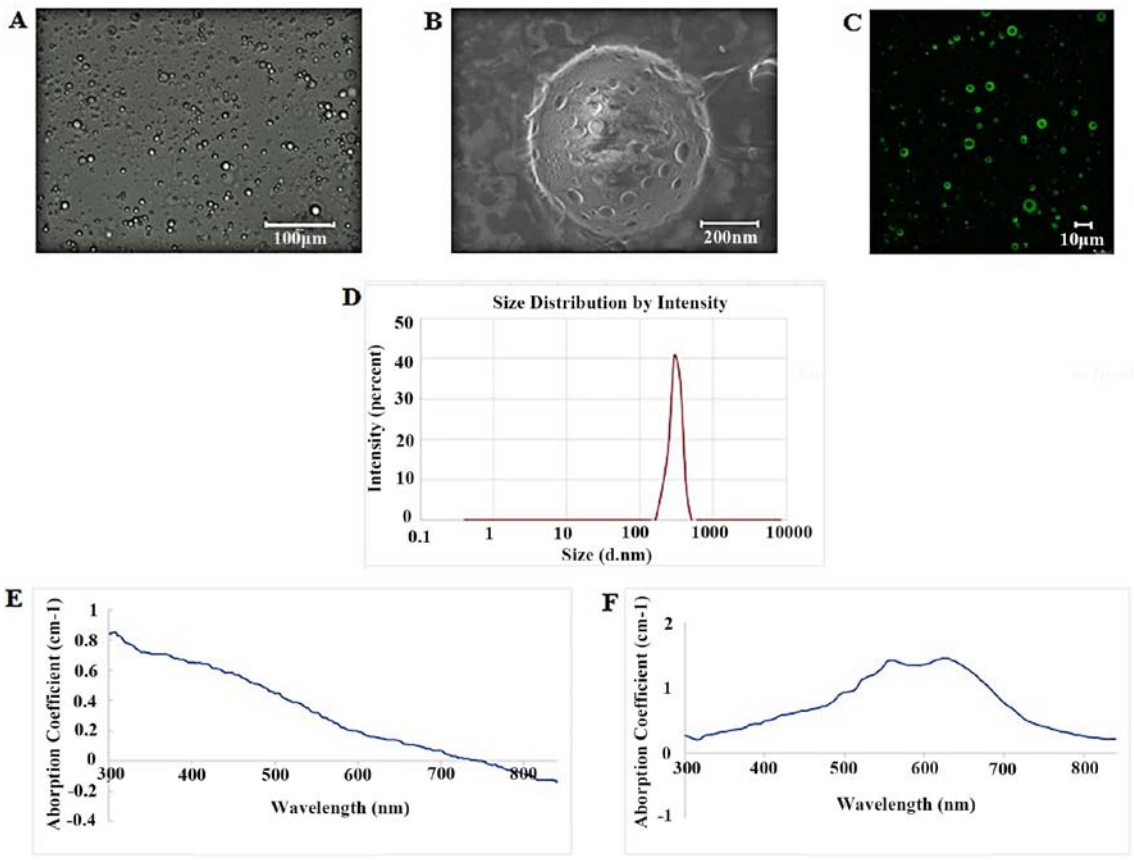

Figure 1. Basic properties of SDF-1/Fe_3O_4/PLGA/PFH nanoparticles. SDF-1/Fe_3O_4/PLGA/PFH nanoparticles were visualized by (A) light, (B) scanning electron and (C) laser confocal microscopy. (D) SDF-1/Fe_3O_4/PLGA/PFH nanoparticle size distribution. (E) Absorption spectra of blank PLGA nanoparticles in the blank control group. (F) Absorption spectra of SDF-1/Fe_3O_4/PLGA/PFH nanoparticles. SDF-1, stromal cell-derived factor 1; Fe_3O_4, iron (II,III) oxide; PLGA, poly(lactic-co-glycolic acid); PFH, fluorocarbon perfluorohexane.

the mean ± standard deviation. Experiments were performed in triplicate. One-way ANOVA followed by Tukey's post hoc test was used to determine significant differences between multiple groups. The Student's t-test was used to analyze differences between two groups The difference between PA signal values of SDF-1/Fe_3O_4/PLGA/PFH and Fe_3O_4/PLGA/PFH nanoparticles was analyzed with unpaired Student's t-test. Difference in EI values of SDF-1/Fe_3O_4/PLGA/PFH nanoparticles before and after the water bath was analyzed using paired Student's t-test. $P<0.05$ was considered to indicate a statistically significant difference.

Results

Basic properties of SDF-1/Fe_3O_4/PLGA/PFH nanoparticles. The nanoparticle solution was dark brown in appearance (data not shown). Under a light or scanning electron microscope, the prepared SDF-1/Fe_3O_4/PLGA/PFH nanoparticles were well dispersed when diluted with pure water, spherical in shape and uniform in size (Fig. 1A and B). Scanning electron microscopy demonstrated that the surfaces of the nanoparticles were incomplete and smooth with numerous pores (Fig. 1B). Laser confocal microscopy indicated that SDF-1 was attached to the PLGA shell of nanoparticles alongside bright green fluorescence on the surface (Fig. 1C). The average size of the nanoparticles, as measured using a Malvern particle size meter, was 586.5±124.7 nm (Fig. 1D) and the average zeta potential was-21.5±2.17 mV. Atomic absorption spectrometry measurements indicated that there was 35.74 μg/ml of iron in the sample (data not shown). UV-Vis spectrophotometry detected 2 slight absorption peaks near 556 and 623 nm for the SDF-1/Fe_3O_4/PLGA/PFH nanoparticles (Fig. 1F), whereas the control group displayed no obvious absorption peaks in detection wavelength bands (Fig. 1E).

PA imaging experiment. UV-V is spectrophotometry was used to detect absorption peaks for the SDF-1/Fe_3O_4/PLGA/PFH nanoparticles at 556 and 623 nm in the wavelength range of 300-840 nm. However, the excitation laser wavelength range of the PA instrument used was 680-960 nm and the absorption peak of the nanoparticles was not within this range. According to its absorption spectrum, 680 nm was selected as the optimal excitation wavelength for the PA imaging experiment. The PA images of 4 groups and the mean PA value of SDF-1/Fe_3O_4/PLGA/PFH and Fe_3O_4/PLGA/PFH groups are presented in Figs. 2 and 3 respectively. The SDF-1/Fe_3O_4/PLGA/PFH and Fe_3O_4/PLGA/PFH nanoparticles displayed obvious PA signals, whereas there were no obvious PA signals from SDF-1/PLGA/PFH or blank PLGA nanoparticles. Furthermore, the PA images of SDF-1/Fe_3O_4/PLGA/PFH and Fe_3O_4/PLGA/PFH nanoparticles were enhanced compared with SDF-1/PLGA/PFH and blank PLGA nanoparticles (Fig. 2) and the average PA signal values of each group significantly increased (Fig. 3) with increasing

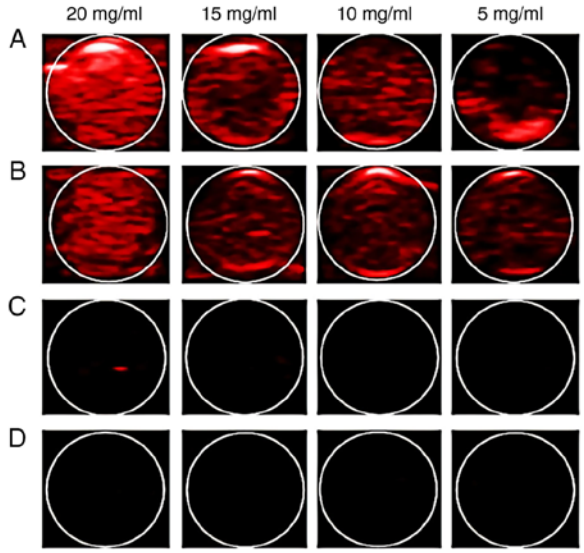

Figure 2. Photoacoustic images of the different groups of nanoparticles at different PLGA concentrations. (A) SDF-1/Fe_3O_4/PLGA/PFH, (B) Fe_3O_4/PLGA/PFH, (C) SDF-1/PLGA/PFH and (D) blank PLGA nanoparticles. PLGA, poly(lactic-co-glycolic acid); SDF-1, stromal cell-derived factor 1; Fe_3O_4, iron (II,III) oxide; PFH, fluorocarbon perfluorohexane.

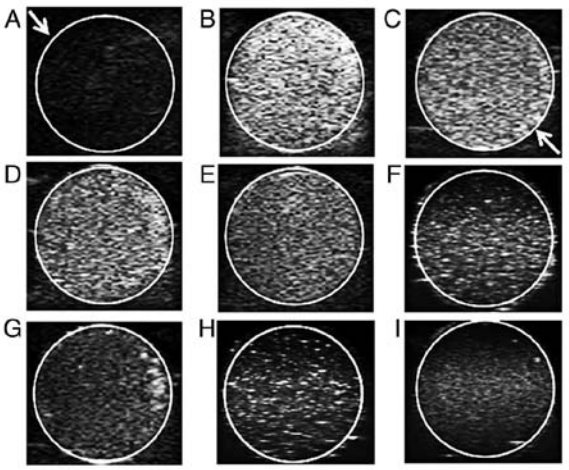

Figure 4. Ultrasonic imaging of SDF-1/Fe_3O_4/PLGA/PFH nanoparticles at different PLGA concentrations and MI values. Images of (A) PBS and SDF-1/Fe_3O_4/PLGA/PFH nanoparticles at PLGA concentrations of (B) 100, (C) 50, (D) 25 and (E) 12.5 mg/ml with a MI of 0.6. Images of SDF-1/Fe_3O_4/PLGA/PFH nanoparticles at MI value of (E) 0.6, (F) 0.5, (G) 0.4, (H) 0.3 and (I) 0.2 at a PLGA concentration of 12.5 mg/ml. Arrows indicate that the ultrasound images are shown within the circles. SDF-1, stromal cell-derived factor 1; Fe_3O_4, iron (II,III) oxide; PLGA, poly(lactic-co-glycolic acid); PFH, fluorocarbon perfluorohexane; MI, mechanical index.

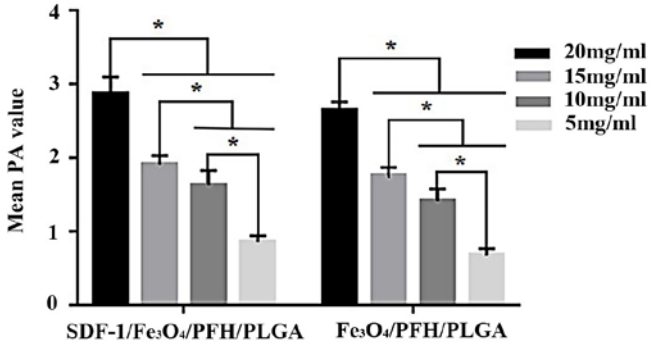

Figure 3. Mean PA signal values of SDF-1/Fe_3O_4/PLGA/PFH and Fe_3O_4/PLGA/PFH nanoparticles. *P<0.05, as indicated. PA, photoacoustic; SDF-1, stromal cell-derived factor 1; Fe_3O_4, iron (II,III) oxide; PLGA, poly(lactic-co-glycolic acid); PFH, fluorocarbon perfluorohexane.

PLGA concentration. Therefore, the results indicated that Fe_3O_4 displayed excellent PA imaging capability and 20 mg/ml nanoparticles emitted the strongest PA signals in the set of nanoparticles.

Ultrasonic imaging experiment. The SDF-1/Fe_3O_4/PLGA/PFH nanoparticles were divided into 4 groups according to PLGA concentration (100, 50, 25 and 12.5 mg/ml) and PBS solution was used as a control group. Samples of the different groups were embedded into an agarose gel model. The ultrasonic mode of the ultrasonic diagnostic instrument and an MI value of 0.6 were used to investigate the imaging conditions of PBS and the different concentrations of nanoparticles (Fig. 4A-E). Furthermore, ultrasound images for 12.5 mg/ml PLGA in nanoparticles with a decreased MI value (0.6 to 0.2) were obtained (Fig. 4E-I). and the corresponding EI values were measured by DFY quantifier. The results demonstrated that when the MI value was constant, the ultrasonic signal displayed a decreasing trend in response to a decrease in nanoparticle concentration (Table I; P<0.05). The PBS solution emitted no obvious ultrasonic signal. Furthermore, when the concentration of nanoparticles was constant, the ultrasonic signal value decreased in response to a decrease in MI (EI values were measured in triplicate for each MI value; Table II; P<0.05). In summary, the ultrasound imaging performance for SDF-1/Fe_3O_4/PLGA/PFH nanoparticles was satisfactory and the EI value was highest when the MI value was 0.6 and the concentration of PLGA was 100 mg/ml.

In vitro phase change experiment. The temperature of the water bath used during the ultrasonic imaging experiment was slowly increased from 37˚C. Images of SDF-1/Fe_3O_4/PLGA/PFH nanoparticles and blank controls were taken before the water bath, when the contrast-enhanced ultrasound imaging was strongest and collected using the contrast mode of the ultrasound diagnostic instrument (Fig. 5). The controls did not display enhanced images; however, the experimental group displayed clear two-dimensional grayscale ultrasound images and contrast-enhanced ultrasound image signals during the heating process. The degree of two-dimensional grayscale ultrasound imaging and contrast-enhanced ultrasound imaging in the experimental group before and after heating, as detected by a DFY quantitative instrument, was significantly increased (grayscale values were measured in triplicate for each image; Table III; P<0.05).

Using an optical microscope, it was observed that nanoparticles were spherical and well dispersed prior to heating (Fig. 6A). Following 1 min in the hot water bath, certain nanoparticles underwent phase transformation and generated microbubbles (Fig. 6B). When the temperature was increased to 56˚C, large amounts of microbubbles with increased volume were observed and the bubbles gradually converged (Fig. 6C). As the temperature continued to increase

Table I. EI values of different PLGA concentrations at a mechanical index of 0.6.

PLGA concentration (mg/ml)	EI
100[a-c]	163.8±3.42
50[a,b]	137.77±1.25
25[a]	116.2±2.98
12.5	99.17±2.76

A decrease in PLGA concentration resulted in significantly decreased EI values in each group. [a]P<0.05 vs. 12.5 mg/ml; [b]P<0.05 vs. 25 mg/ml; [c]P<0.05 vs. 50 mg/ml. EI, echo density; PLGA, poly(lactic-co-glycolic acid).

Table II. EI values of different MIs at a concentration of 12.5 mg/ml PLGA.

MI	EI
0.6[a-d]	99.17±2.76
0.5[a-c]	78.96±3.15
0.4[a,b]	66.25±2.36
0.3[a]	54.59±2.42
0.2	43.73±2.59

A decrease in MI resulted in significantly decreased EI values in each group. [a]P<0.05 vs. 0.2 MI; [b]P<0.05 vs. 0.3 MI; [c]P<0.05 vs. 0.4 MI; [d]P<0.05 vs. 0.5 MI. EI, echo density; MI, mechanical index; PLGA, poly(lactic-co-glycolic acid).

to 65˚C, the microbubbles gradually burst and disappeared (data not shown).

Detection of CXCR4 localization and expression in SCC-15 cells. In Fig. 7, blue indicated the nuclei of SCC-15 cells re-stained with DAPI and green indicated CXCR4 labeled with FITC (as indicated by arrows). The target protein was expressed in the cell membrane and cytoplasm, which indicated that CXCR4 was an ideal membrane target protein.

Targeted experiment with SCC-15 cells. SCC-15 cells were observed under a light microscope and were found to exhibit a tadpole-shaped morphology and were evenly distributed (Fig. 8A). Following SDF-1/Fe_3O_4/PLGA/PFH nanoparticle addition and incubation for 2 h, SCC-15 cells were observed under a light microscope. A large number of nanoparticles adhered around SCC-15 cell membranes and to the cytoplasm (Fig. 8B). A fully-automatic fluorescence pattern of Fig. 8B from the same view was generated and bright green fluorescence was observed in and around the SCC-15 cells (as indicated by the arrows; Fig. 8C). The results demonstrated that SDF-1/Fe_3O_4/PLGA/PFH nanoparticles specifically bound to CXCR4 in SCC-15 cells.

Flow cytometry test. The rate of binding of the targeted nanoparticle group to SCC-15 cells was 84.44%, while that of the controls was only 1.1%. The results indicated that the nanoparticles possessed strong targeted binding ability to SCC-15 cells (Fig. 9).

Discussion

In the present study, a double emulsification method was used to prepare multifunctional, targeted polymeric nanoparticles using PLGA as the carrier. PLGA contains rich functional groups that can promote functionalization of PLGA-based nanoparticles and biomolecules, and can improve their stability and functionality (17). PFH and Fe_3O_4 were used concurrently as a coating and the surface of the PGLA shell was linked to FITC-labeled SDF-1 via thioether bonds, thus forming a nanoparticle with multiple functions.

The physical characteristics of the particles were tested using various methods. The solution of the nanoparticles was observed to be dark brown to the naked eye and the nanoparticles appeared round and spherical with numerous surface pores when observed via scanning electron microscopy. The particle size was measured to be 586.48±124.70 nm. It has been reported that the microvascular endothelial gap in SCC is 300-780 nm (30); therefore, the nanoparticles could potentially pass through the microvascular endothelial gap and be deposited into the target tissue via the CXCR4-CXCL12 axis. The therapeutic application of the nanoparticles may aid in locating tumors and metastatic lymphoma more accurately and blocking further metastasis via these channels. Contrary to the structure of tumor tissue, the vascular endothelium of normal tissue is tightly connected and extravasation of nanoparticles is not possible; however, tumors display enhanced vascular permeability and poor lymph drainage, which facilitates the retention of nanoparticles that extravasate into tumor tissue for a prolonged time (37).

Multi-modal imaging has served an increasingly important role in medical diagnosis and increased focused research on numerous multi-modality contrast agents with multiple imaging functions has been conducted (38). With the rapid development of medical imaging technology, ultrasound, computed tomography (CT), X-rays and MR imaging have been widely used. Imaging technology can be used for molecular and functional imaging of target organs and tissues to obtain pathological information, thus aiding in the early diagnosis of diseases (39). MR is frequently used to diagnose breast cancer (40) and CT is often used for localized brain tumors, head and neck cancer, and multiple myeloma (41). However, the imaging techniques currently used in clinical practice have limitations, including missed diagnosis, misdiagnosis and they are not specific to or target lesions (8).

PA imaging is a novel biomedical imaging mode that combines the advantages of optics and acoustics to improve the spatial resolution of traditional ultrasound (30). Combining data from two or more imaging techniques can improve diagnosis accuracy (42).

Fe_3O_4, a photosensitive material, absorbs laser light of a specific wavelength and causes the ambient temperature to rise (31). The thermal expansion of the surrounding objects produces a PA effect and the signal device generates PA signals after receiving sound waves (32). Simultaneously, Fe_3O_4 magnetic particles can vibrate in response to acoustic waves, altering the acoustic impedance of surrounding tissues and enhancing ultrasonic development (43). Additionally, numerous experimental studies have demonstrated that Fe_3O_4

Table III. Grayscale values before and after the water bath in the experimental group.

Temperature	Two-dimensional grayscale ultrasound imaging	Contrast-enhanced ultrasound imaging
Before (37˚C)	68±1.73	32±1.67
After (56˚C)	152±2.75[a]	101±3.09[a]

[a]P<0.05 vs. before.

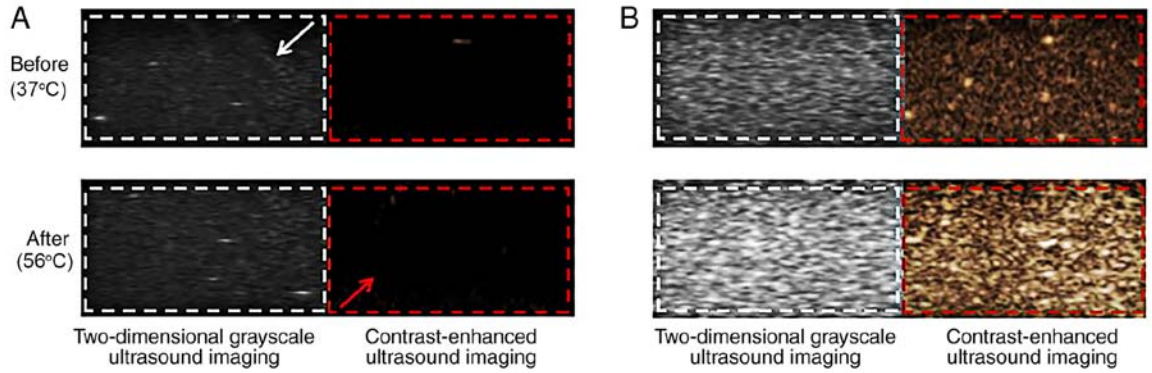

Figure 5. Two-dimensional grayscale ultrasound imaging and contrast-enhanced ultrasound imaging of SDF-1/Fe_3O_4/PLGA/PFH nanoparticles and controls. (A) Blank PLGA and (B) SDF-1/Fe_3O_4/PLGA/PFH nanoparticles. Two-dimensional grayscale ultrasound images are displayed within the white dotted frame (as indicated by the white arrow). Contrast-enhanced ultrasound images are presented within the red dotted frame (as indicated by the red arrow). SDF-1, stromal cell-derived factor 1; Fe_3O_4, iron (II,III) oxide; PLGA, poly(lactic-co-glycolic acid); PFH, fluorocarbon perfluorohexane.

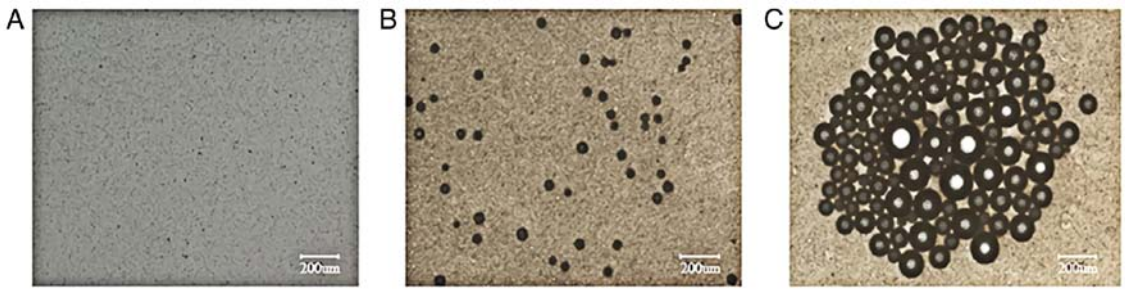

Figure 6. Images of SDF-1/Fe_3O_4/PLGA/PFH nanoparticles before and after water bath treatment. (A) Nanoparticles before the water bath. (B) Following 1 min in the water bath, certain nanoparticles underwent phase transformation and generated microbubbles. (C) When the temperature of the water bath reached ~56˚C, a large amount of microbubbles converged. SDF-1, stromal cell-derived factor 1; Fe_3O_4, iron (II,III) oxide; PLGA, poly(lactic-co-glycolic acid); PFH, fluorocarbon perfluorohexane.

improves the transverse relaxation rate of MR and improves MR imaging capability (44-46). Fe_3O_4 can integrate enhanced PA ultrasound and MR imaging, is an ideal molecular imaging material and is biodegradable and safe (21). After entering the body, Fe_3O_4 is metabolized by red blood cells and enters the normal plasma iron pool to participate in the synthesis of hemoglobin, myoglobin and cytochrome oxidase, or participate in energy metabolism and hematopoietic functions (47). In the *in vitro* imaging experiments performed in the present study, the Fe_3O_4-coated nanoparticles displayed PA and ultrasound imaging capabilities, which indicated that they may serve as a multi-modal contrast agent with potential clinical use for lesion visualization.

PFH is liquid at normal temperature, but when the temperature rises to its boiling point (56˚C) or above, or the external pressure decreases to its gasification pressure threshold, a liquid-gas phase change occurs (6). When PFH enters the gas phase, the increase of microsphere volume results in the increase of acoustic impedance, then ultrasonic development is enhanced (48). Commonly used methods to promote liquid-gas phase transition of liquid fluorocarbon include temperature-induced phase change (49), acoustic droplet vaporization (50,51) and optical droplet vaporization (32). In the present study, a water bath heating method was used to induce PFH liquid-gas phase change. When the temperature rose to ~56˚C, numerous phase change microbubbles were observed using a microscope. Additionally, the EI values of two-dimensional grayscale and contrast-enhanced ultrasound images were significantly increased compared with before heating in the water bat (37˚C). When the temperature rose to 65˚C, the microbubbles burst and disappeared, weakening the image. As the phase change temperature

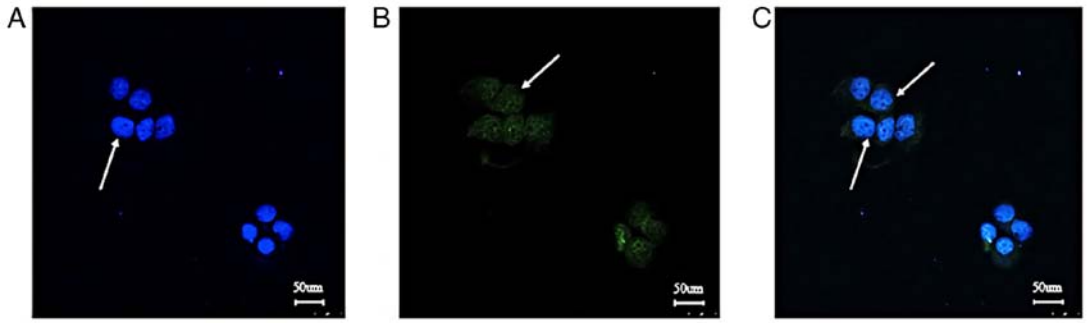

Figure 7. Immunofluorescence assay of SCC-15 cells. (A) The nuclei of SCC-15 cells were stained with DAPI, as indicated by the white arrow. (B) CXC chemokine receptor 4 was stained with FITC, as indicated by the white arrow. (C) Merged image.

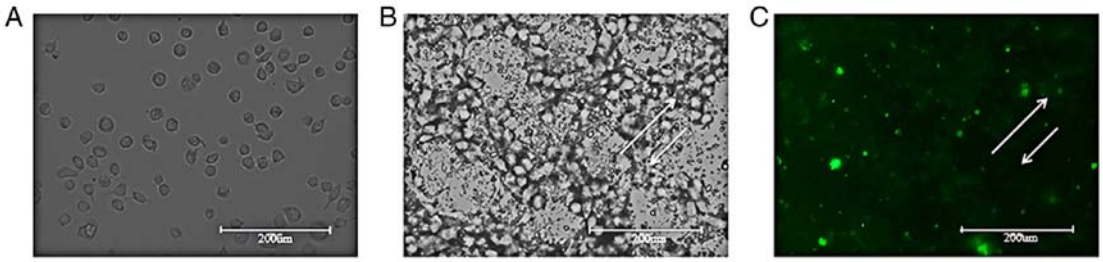

Figure 8. Targeted experiments with SCC-15 cells and SDF-1/Fe_3O_4/PLGA/PFH. (A) SCC-15 cells without nanoparticles. (B) Light microscope image of SCC-15 cells with nanoparticles. (C) Fluorescence microscope image of SCC-15 cells with nanoparticles. SDF-1, stromal cell-derived factor 1; Fe_3O_4, iron (II,III) oxide; PLGA, poly(lactic-co-glycolic acid); PFH, fluorocarbon perfluorohexane. The SDF-1/Fe_3O_4/PLGA/PFH nanoparticles bind specifically to SCC-15 cells, as indicated by the white arrows.

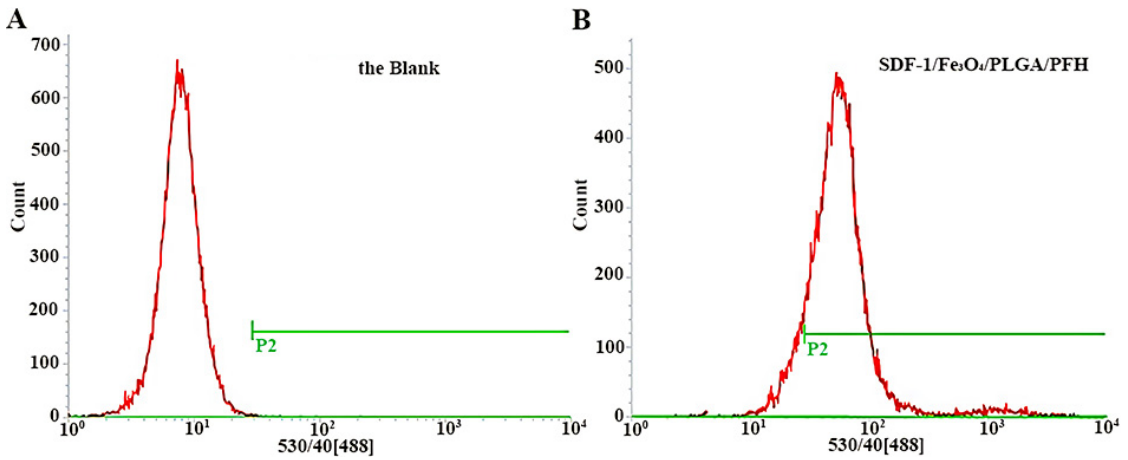

Figure 9. Flow cytometric analysis of SDF-1/Fe_3O_4/PLGA/PFH nanoparticles. Blank control nanoparticles and SDF-1/Fe_3O_4/PLGA/PFH nanoparticles. SDF-1, stromal cell-derived factor 1; Fe_3O_4, iron (II,III) oxide; PLGA, poly(lactic-co-glycolic acid); PFH, fluorocarbon perfluorohexane.

of PFH is higher than the body temperature of the human body, an external water bath heating was used to promote the phase change; however, this would be difficult to implement in the human body. Fe_3O_4, a photosensitive material, can undergo photo-thermal conversion under laser radiation to increase the temperature of the surrounding medium, which may serve as a potential mechanism to promote PFH phase change in the body (52). Moreover, a laser has stability and directionality, and can treat tumors without damaging the surrounding normal tissues via the principle of thermal ablation, thus providing a direction for future *in vivo* experiments (6).

SCC of the tongue accounts for the majority of oral SCC cases and its high lymph node metastasis rate results in the low 5-year survival rate (<30%) of patients (53). Several studies have reported that CXCR4 is widely and highly expressed in oral SCC cells, including SCC cells of the tongue (30,54,55). Additionally, it has been demonstrated that the CXCR4-CXCL12 axis serves an important role in the proliferation, invasion, immune evasion and metastasis of several types of cancer, including oral SCC (56,57). The interaction between CXCR12 and its receptor stimulates downstream signaling pathways to affect tumor angiogenesis, tumor cell proliferation and chemical resistance, which suggest that CXCR12 may serve as a potential target for

cancer therapy (58). More importantly, when SDF-1 on targeted nanoparticles combines with CXCR4, it can antagonize the tumor-promoting effect caused by CXCR4-SDF-1 (36). The active targeting effect of SDF-1 allows nanoparticles to remain in tumor tissues for a prolonged time and allows the rapid release of drugs using laser local fixed-point radiation, which would increase local drug concentrations and achieve a chemotherapy effect while reducing systemic adverse reactions; therefore, the aforementioned strategy may be used for targeted treatment with long-term chemotherapy drugs (6). Cellular immunofluorescence experiments demonstrated that CXCR4 is expressed in the cell membrane and cytoplasm of SCC-15 cells and is an ideal membrane protein target. In the present study, SDF-1 was attached to a PLGA shell by a thioether bond and SDF-1/Fe_3O_4/PLGA/PFH nanoparticles were successfully generated. SCC-15 targeting experiments indicated that SDF-1/Fe_3O_4/PLGA/PFH nanoparticles specifically combined with CXCR4 in SCC-15 cells and bright green fluorescence was microscopically observed in and around the cells. Flow cytometry assays indicated that the generated nanoparticles displayed a high targeting ability. However, whether the expected target effect can be achieved *in vivo* requires further investigation.

In the present study, a targeted nanoparticle contrast agent with a PA/ultrasonic bimodal imaging function was successfully generated. Basic physical characteristics of the nanoparticles were studied *in vitro* and it displayed PA and ultrasonic imaging capabilities. The nanoparticles underwent *in vitro* phase change under certain conditions to enhance ultrasonic imaging and specific adherence to tongue SCCs *in vitro*. The present work provided support for establishing procedures and standards to be used for the diagnosis of primary foci of tongue carcinoma and metastatic SCC of the lymph nodes and established a foundation for subsequent *in vivo* experiments.

Acknowledgements

Not applicable.

Funding

The present study was funded by the Chongqing Social Livelihood Science and Technology Innovation Project (grant no. cstc2016shmszx00010), the Science and Technology Research Project of Chongqing Education Commission (grant no. KJ1600231) and the Program for Innovation Team Building at Institutions of Higher Education in Chongqing (grant no. CXTDG201602006).

Availability of data and materials

The datasets used and/or analyzed during the current study are available from the corresponding author on reasonable request.

Authors' contributions

FW performed the majority of the experiments and wrote the manuscript. ZW, LP and SW analyzed and interpreted data. LQ designed and supervised the study. All authors read and approved the final manuscript.

Ethics approval and consent to participate

Not applicable.

Patient consent for publication

Not applicable.

Competing interests

The authors declare that they have no competing interests.

References

1. Chen X, Xu WH, Zhou J and Wang YL: Current situation of oral squamous cell carcinoma. Stomatology 37: 462-465, 2017.
2. Chen F, Yan L, Lin L, Liu F, Qiu Y, Wang J, Wu J, Liu F, Huang J, Cai L, *et al*: Dietary score and the risk of oral cancer: A case-control study in southeast China. Oncotarget 8: 34610-34616, 2017.
3. Deshpande N, Needles A and Willmann JK: Molecular ultrasound imaging: Current status and future directions. Clin Radiol 65: 567-581, 2010.
4. Riemann M, Knipfer C, Rohde M, Alder W, Schuster M, Noeth E, Oetter N, Shams N, Neukam FW and Stelzlle F: Oral squamous cell carcinoma of the tongue: Prospective and objective speech evaluation of patients undergoing surgical therapy. Head Neck 38: 993-1001, 2016.
5. Chang CC, Yang YJ, Li YJ, Chen ST, Lin BR, Wu TS, Lin SK, Kuo MY and Tan CT: Corrigendum to 'MicroRNA-17/20a functions to inhibit cell migration and can be used a prognostic marker in oral squamous cell carcinoma' [Oral Oncol. 49(9) (2013) 923-931]. Oral Oncol 72: 202-203, 2017.
6. Xiong J, Feng J, Qiu L, Gao Z, Li P, Pang L and Zhang Z: SDF-1-loaded PLGA nanoparticles for the targeted photoacoustic imaging and photothermal therapy of metastatic lymph nodes in tongue squamous cell carcinoma. Int J Pharm 554: 93-104, 2019.
7. Hwang-Bo J, Bae MG, Park JH and Chung IS: 3-O-Acetyloleanolic acid inhibits VEGF-A-induced lymphangiogenesis and lymph node metastasis in an oral cancer sentinel lymph node animal model. BMC Cancer 18: 714, 2018.
8. Zhang X, Zhang L, Tan X, Lin Y, Han X, Wang H, Ming H, Li Q, Liu K and Feng G: Systematic analysis of genes involved in oral cancer metastasis to lymph nodes. Cell Mol Biol Lett 23: 53, 2018.
9. Szaniszlo P, Fennewald SM, Qiu S, Kantara C, Shilagard T, Vargas G and Resto VA: Temporal characterization of lymphatic metastasis in an orthotopic mouse model of oral cancer. Head Neck 36: 1638-1647, 2014.
10. Wei W, Jiang D, Rosenkrans ZT, Barnhart TE, Engle JW, Luo Q and Cai W: HER2-targeted multimodal imaging of anaplastic thyroid cancer. Am J Cancer Res 9: 2413-2427, 2019.
11. Xue LY, Jiang ZY, Fu TT, Wang QM, Zhu YL, Dai M, Wang WP, Yu JH and Ding H: Transfer learning radiomics based on multimodal ultrasound imaging for staging liver fibrosis. Eur Radiol 30: 2973-2983, 2020.
12. Rapoport N, Christensen DA, Kennedy AM and Nam KH: Cavitation properties of block copolymer stabilized phase-shift nanoemulsions used as drug carriers. Ultrasound Med Biol 36: 419-429, 2010.
13. Niu C, Wang Z, Lu G, Krupka TM, Sun Y, You Y, Song W, Ran H, Li P and Zheng Y: Doxorubicin loaded superparamagnetic PLGA-iron oxide multifunctional microbubbles for dual-mode US/MR imaging and therapy of metastasis in lymph nodes. Biomaterials 34: 2307-2317, 2013.
14. Li A, Zheng Y, Yu J, Wang Z, Yang Y, Wu W, Guo D and Ran H: Superparamagnetic perfluorooctylbromide nanoparticles as a multimodal contrast agent for US, MR, and CT imaging. Acta Radiol 54: 278-283, 2013.
15. Jain RA: The manufacturing techniques of various drug loaded biodegradable poly(lactide-co-glycolide) (PLGA) devices. Biomaterials 21: 2475-2490, 2000.

16. Li P, Zheng Y, Ran H, Tan J, Lin Y, Zhang Q, Ren J and Wang Z: Ultrasound triggered drug release from 10-hydroxycamptothecin-loaded phospholipid microbubbles for targeted tumor therapy in mice. J Control Release 162: 349-354, 2012.
17. Ao M, Wang Z, Ran H, Guo D, Yu J, Li A, Chen W, Wu W and Zheng Y: Gd-DTPA-loaded PLGA microbubbles as both ultrasound contrast agent and MRI contrast agent-a feasibility research. J Biomed Mater Res B Appl Biomater 93: 551-556, 2010.
18. Lowe KC: Engineering blood: Synthetic substitutes from fluorinated compounds. Tissue Eng 9: 389-399, 2003.
19. Cyrus T, Winter PM, Caruthers SD, Wickline SA and Lanza GM: Magnetic resonance nanoparticles for cardiovascular molecular imaging and therapy. Expert Rev Cardiovasc Ther 3: 705-715, 2005.
20. Tural B, Ozenbaş M, Atalay S and Volkan M: Rapid synthesis and characterization of maghemite nanoparticles. J Nanosci Nanotechnol 8: 861-866, 2008.
21. Sun Y, Zheng Y, Ran H, Zhou Y, Shen H, Chen Y, Chen H, Krupka TM, Li A, Li P, *et al*: Superparamagnetic PLGA-iron oxide microcapsules for dual-modality US/MR imaging and high intensity focused US breast cancer ablation. Biomaterials 33: 5854-5864, 2012.
22. Qiao RR, Yang CH and Gao MY: Superparamagnetic iron oxide nanoparticles: From preparations to in vivo MRI applications. J Mater Chem 19: 6274-6293, 2009.
23. Mu X, Zhang F, Kong C, Zhang H, Zhang W, Ge R, Liu Y and Jiang J: EGFR-targeted delivery of DOX-loaded Fe_3O_4@ polydopamine multifunctional nanocomposites for MRI and antitumor chemo-photothermal therapy. Int J Nanomedicine 12: 2899-2911, 2017.
24. Liu ZY, Wang Y, Liang CH, Li XH, Wang GY, Liu HJ and Li Y: In vitro labeling of mesenchymal stem cells with superparamagnetic iron oxide by means of microbubble-enhanced US exposure: Initial experience. Radiology 253: 153-159, 2009.
25. Degen CL, Poggio M, Mamin HJ, Rettner CT and Rugar D: Nanoscale magnetic resonance imaging. Proc Natl Acad Sci USA 106: 1313-1317, 2009.
26. Jun YW, Lee JH and Cheon J: Chemical design of nanoparticle probes for high-performance magnetic resonance imaging. Angew Chem Int Ed Engl 47: 5122-5135, 2008.
27. Norton SJ and Vo-Dinh T: Imaging the distribution of magnetic nanoparticles with ultrasound. IEEE Trans Med Imaging 26: 660-665, 2007.
28. Chen ZJ, Yang SH and Xing D: In vivo detection of hemoglobin oxygen saturation and carboxyhemoglobin saturation with multiwavelength photoacoustic microscopy. Opt Lett 37: 3414-3416, 2012.
29. Ermilov SA, Khamapirad T, Conjusteau A, Leonard MH, Lacewell R, Mehta K, Miller T and Oraevsky AA: Laser optoacoustic imaging system for detection of breast cancer. J Biomed Opt 14: 024007, 2009.
30. Li C and Wang LV: Photoacoustic tomography and sensing in biomedicine. Phys Med Biol 54: R59-R97, 2009.
31. Grootendorst DJ, Jose J, Fratila RM, Visscher M, Velders AH, Ten Haken B, Van Leeuwen TG, Steenbergen W, Manohar S and Ruers TJ: Evaluation of superparamagnetic iron oxide nanoparticles (Endorem®) as a photoacoustic contrast agent for intra-operative nodal staging. Contrast Media Mol Imaging 8: 83-91, 2013.
32. Strohm E, Rui M, Gorelikov I, Matsuura N and Kolios M: Vaporization of perfluorocarbon droplets using optical irradiation. Biomed Opt Express 2: 1432-1442, 2011.
33. Balkwill F: The significance of cancer cell expression of the chemokine receptor CXCR4. Semin Cancer Biol 14: 171-179, 2004.
34. Delilbasi CB, Okura M, Iida S and Kogo M: Investigation of CXCR4 in squamous cell carcinoma of the tongue. Oral Oncol 40: 154-157, 2004.
35. Lee DJ, Lyshchik A, Huamani J, Hallahan DE and Fleischer AC: Relationship between retention of a vascular endothelial growth factor receptor 2 (VEGFR2)-targeted ultrasonographic contrast agent and the level of VEGFR2 expression in an in vivo breast cancer model. J Ultrasound Med 27: 855-866, 2008.
36. Mei L, Liu Y, Zhang Q, Gao HL, Zhang Z and He Q: Enhanced antitumor and anti-metastasis efficiency via combined treatment with CXCR4 antagonist and liposomal doxorubicin. J Control Release 196: 324-331, 2014.
37. Iyer AK, Khaled G, Fang J and Maeda H: Exploiting the enhanced permeability and retention effect for tumor targeting. Drug Discov Today 11: 812-818, 2006.
38. Ke H, Yue X, Wang J, Xing S, Zhang Q, Dai Z, Tian J, Wang S and Jin Y: Gold nanoshelled liquid perfluorocarbon nanocapsules for combined dual modal ultrasound/CT imaging and photothermal therapy of cancer. Small 10: 1220-1227, 2014.
39. Zhigang W, Zhiyu L, Haitao R, Hong R, Qunxia Z, Ailong H, Qi L, Chunjing Z, Hailin T, Lin G, *et al*: Ultrasound-mediated microbubble destruction enhances VEGF gene delivery to the infarcted myocardium in rats. Clin Imaging 28: 395-398, 2004.
40. Kuhl CK, Strobel K, Bieling H, Leutner C, Schild HH and Schrading S: Supplemental breast MR imaging screening of women with average risk of breast cancer. Radiology 283: 361-370, 2017.
41. Ell PJ: PET/CT in oncology: A major technology for cancer care. Chang Gung Med J 28: 274-283, 2005.
42. Razansky D, Buehler A and Ntziachristos V: Volumetric real-time multispectral optoacoustic tomography of biomarkers. Nat Protoc 6: 1121-1129, 2011.
43. Liu Z, Lammers T, Ehling J, Fokong S, Bornemann J, Kiessling F and Gätjens J: Iron oxide nanoparticle-containing microbubble composites as contrast agents for MR and ultrasound dual-modality imaging. Biomaterials 32: 6155-6163, 2011.
44. Kim J, Park S, Lee JE, Jin SM, Lee JH, Lee IS, Yang I, Kim JS, Kim SK, Cho MH and Hyeon T: Designed fabrication of multifunctional magnetic gold nanoshells and their application to magnetic resonance imaging and photothermal therapy. Angew Chem Int Ed Engl 45: 7754-7758, 2006.
45. Tian Q, Hu J, Zhu Y, Zou R, Chen Z, Yang S, Li R, Su Q, Han Y and Liu X: Sub-10 nm Fe3O4@Cu(2-x)S core-shell nanoparticles for dual-modal imaging and photothermal therapy. J Am Chem Soc 135: 8571-8577, 2013.
46. Ling Y, Wei K, Luo Y, Gao X and Zhong S: Dual docetaxel/superparamagnetic iron oxide loaded nanoparticles for both targeting magnetic resonance imaging and cancer therapy. Biomaterials 32: 7139-7150, 2011.
47. Duguet E, Vasseur S, Mornet S and Devoisselle JM: Magnetic nanoparticles and their applications in medicine. Nanomedicine (Lond) 1: 157-168, 2006.
48. Chen YL, Liu FQ, Guo Y, Cheng J, Yang L, Lu M, Li P, Xu J, Yu T, Wang ZG, *et al*: PA/US dual-modality imaging to guide VEGFR-2 targeted photothermal therapy using ZnPc-/PFH-loaded polymeric nanoparticles. Biomater Sci 6: 2130-2143, 2018.
49. Huang JW, Xu JS, Schmidt C and Xu RX: Heat sensitive microbubbles for intraoperative assessment of cancer ablation margin. Multimodal biomedical imaging VII. Int Soc Opt Photonics 8216: 821604, 2012.
50. Zhou Y, Wang Z, Chen Y, Shen H, Luo Z, Li A, Wang Q, Ran H, Li P, Song W, *et al*: Microbubbles from gas-generating perfluorohexane nanoemulsions for targeted temperature-sensitive ultrasonography and synergistic HIFU ablation of tumors. Adv Mater 25: 4123-4130, 2013.
51. Xu S, Zong Y, Li W, Zhang S and Wan M: Bubble size distribution in acoustic droplet vaporization via dissolution using an ultrasound wide-beam method. Ultrason Sonochem 21: 975-983, 2014.
52. Chu M, Shao Y, Peng J, Dai X, Li H, Wu Q and Shi D: Near-infrared laser light mediated cancer therapy by photothermal effect of Fe3O4 magnetic nanoparticles. Biomaterials 34: 4078-4088, 2013.
53. Sano D and Myers JN: Metastasis of squamous cell carcinoma of the oral tongue. Cancer Metastasis Rev 26: 645-662, 2007.
54. Oliveira-Neto HH, Silva ET, Leles CR, Mendonca EF, Alencar Rde C, Silva TA and Batista AC: Involvement of CXCL12 and CXCR4 in lymph node metastases and development of oral squamous cell carcinomas. Tumour Biol 29: 262-271, 2008.
55. Almofti A, Uchida D, Begum NM, Tomizuka Y, Iga H, Yoshida H and Sato M: The clinicopathological significance of the expression of CXCR4 protein in oral squamous cell carcinoma. Int J Oncol 25: 65-71, 2004.
56. Teicher BA and Fricker SP: CXCL12 (SDF-1)/CXCR4 pathway in cancer. Clin Cancer Res 16: 2927-2931, 2010.
57. Rave-Fränk M, Tehrany N, Kitz J, Leu M, Weber HE, Burfeind P, Schliephake H, Canis M, Beissbarth T, Reichardt HM and Wolff HA: Prognostic value of CXCL12 and CXCR4 in inoperable head and neck squamous cell carcinoma. Strahlenther Onkol 192: 47-54, 2016.
58. Meng W, Xue S and Chen Y: The role of CXCL12 in tumor microenvironment. Gene 641: 105-110, 2018.